(LAMC-1149) AECD-3396

SECRET
SECURITY INFORMATION

54702

CLASSIFICATION CANCELLED
DATE 5-19-52
For The Atomic Energy Commission
Wilhelmina C. Hemmer
Chief, Declassification Branch

THIS DOCUMENT CONSISTS OF 58 PAGE(S)
NO 8 OF 14 COPIES, SERIES A

39536

Limiting Conditions for Jet Formation in High Velocity Collisions

W.O.-24212

LAB-GMX6-84

March 27, 1952

Distribution:

Written by:
J. M. Walsh
R. G. Shreffler
F. J. Willig

SECRET
SECURITY INFORMATION

ABSTRACT

The high-velocity collision of two solids is discussed as a problem in compressible fluid hydrodynamics. Such collisions may conveniently be divided into jetless and jet-forming categories. A theory is presented which describes flow in the collision region for the jetless case, and determines a critical collision angle (as a function of material velocities and equation-of-state properties of the materials) above which a jet must arise from the collision.

The experimental study of solid collisions utilizes metal plates driven by high explosives, the collision process being recorded with a high-speed smear camera. Two experimental arrangements are used, and data for collisions employing dural, mild steel, brass and lead are presented. Jetless and jet-forming collisions are observed, and critical angles separating the two types are compared with theoretical predictions. Agreement seems satisfactory to indicate that the theory is valid.

Introduction

The collision of two solids gives rise to internal pressures in the vicinity of the collision. Pressures resulting from an extremely violent collision may be sufficiently high that the strength of the material is negligible, so that motion in the collision region can be treated as a problem in compressible fluid hydrodynamics. Velocities adequate for such collisions may be attained, for example, by accelerating metal plates by means of high explosive charges.

It is the purpose of the present paper to discuss such collisions. The symmetric collision of two identical plates, illustrated in Fig. 1, will be emphasized. While specialization to symmetric collisions provides some gain in simplicity, generalizations to asymmetric collisions of both theoretical and experimental work are straightforward and are indicated in the discussion. Fig. 1A, the collision referred to a laboratory system of coordinates, gives the nomenclature used. The coalesced plates are called a slug, and the forward stream of material, often observed in such collisions, is called a jet. Slug, jet and the instantaneous collision region all move to the right in this system of coordinates. For some purposes, it is convenient to refer motion to a moving reference system in which the collision region is stationary; the flow configuration then becomes that of the two impinging streams illustrated in Figure 1B.

Two complementary theories of the collision process, treated as problems in compressible hydrodynamics, are discussed below.

Fig. 1A. The symmetric collision of two plates, referred to a laboratory system of coordinates.

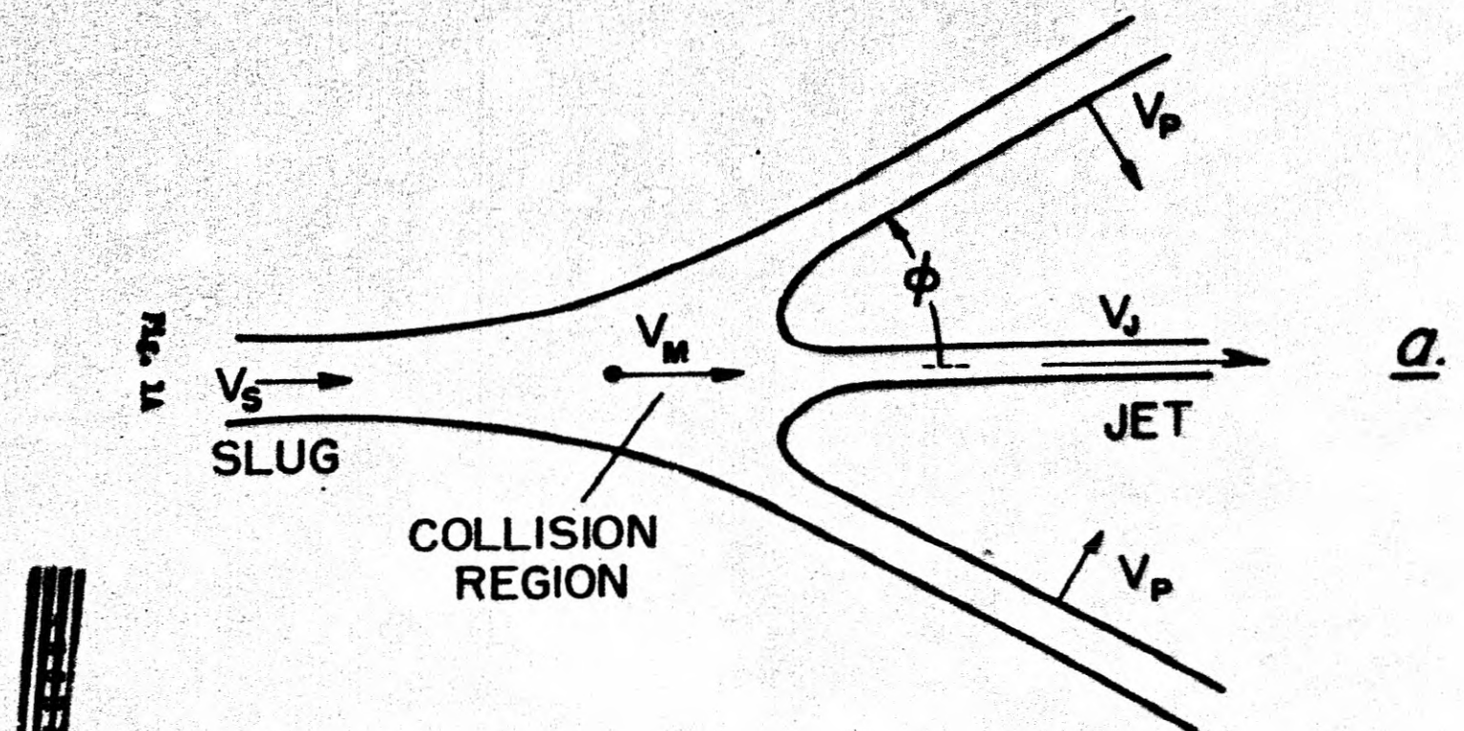

a.

Fig. 1B. The symmetric collision of two plates, referred to a coordinate system moving with the collision region.

b.

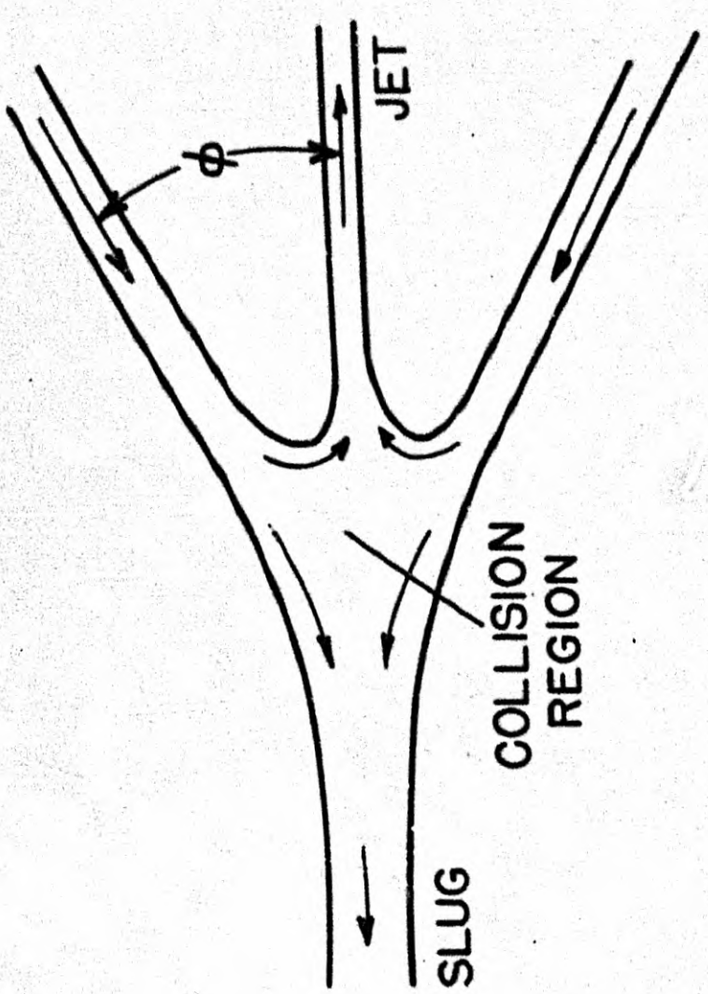

Fig. 1B

Experiments which accomplish the desired collisions are described, and experimental data are compared with the theories.

Theory

A shockless treatment of the collision problem, adequate for many important applications, has appeared in the literature[1]. The problem was treated as one in the classical hydrodynamics of a compressible perfect fluid, and the role of shock waves within the flow was ignored. With these assumptions, the following equations describing the jet and slug were obtained:

$$V_j = \frac{V_p}{\sin \varphi} (1 + \cos \varphi) \qquad (1)$$

$$V_s = \frac{V_p}{\sin \varphi} (1 - \cos \varphi) \qquad (2)$$

$$M_j = \frac{M}{2} (1 - \cos \varphi) \qquad (3)$$

$$M_s = \frac{M}{2} (1 + \cos \varphi) \qquad (4)$$

M, M_j and M_s are mass per unit time of material flowing into the collision region, the jet and the slug, respectively. The remaining symbols are illustrated in Fig. 1. Eqn. (1) is valuable in the interpretation of experiments described in later paragraphs. It may be noted that this equation, if applied in an unrestricted manner to all collisions, would indicate a jet velocity which

(1) Garrett Birkhoff, Duncan P. MacDougall, Emerson Pugh and Sir Geoffrey Taylor. "Explosives with Lined Cavities" J. Appl. Phys. 19 563-582 (1948).

approaches infinity as ε approaches zero.

For collisions in which the angle 2ε between the free surfaces is small, the flow may be different from that depicted in the theory above. The jetless configuration[2], postulated for an infinitesimal region about the point of collision M, is shown in Fig. 2; motion is referred to a coordinate system in which the point of collision is stationary, as in Fig. 1B. For supersonic entry flow, U_0, with ε sufficiently small, stationary shocks are possible which straighten the impinging streams and cause them to coalesce without emitting a forward jet. Although this flow is postulated for $\varepsilon < \varepsilon_c$, a few remarks indicate it to be the only plausible jetless configuration: Since, by hypothesis, U_0 is supersonic, it follows that a sonic disturbance from the collision cannot remain stationary in the entry flow. The flow must, then, first encounter a shock wave. If such a shock wave is ahead of M, however, the pressure behind the shock will be released at the free surface by flow of fluid into the cavity, and jetting results. Excluding disturbances ahead of M, a discontinuity (shock) at M must exist, since a discontinuous change in flow direction is required by the boundary condition that flow cannot cross the line of symmetry BM. Finally, if the deflection ε is to be accomplished in stages by two or more shocks through M, one finds that the component of flow normal to the second shock is always subsonic, which is impossible. The deflection ε, then, if the configuration is to be jetless, must be accomplished by a single shock through M, as indicated in Fig. 2.

(2) This notion was first conceived by K. Fuchs and P. Stein, Los Alamos Scientific Laboratory (1945). The treatment given here more closely follows the earlier work of A. Busemann, Gas dynamik, Handbuch der Experimentalphysik, Vol. IV, (1931).

Fig. 2. Postulated jetless configuration for the symmetric collision. The flow is for an infinitesimal region about the point of collision, M, and is referred to a coordinate system in which M is motionless.

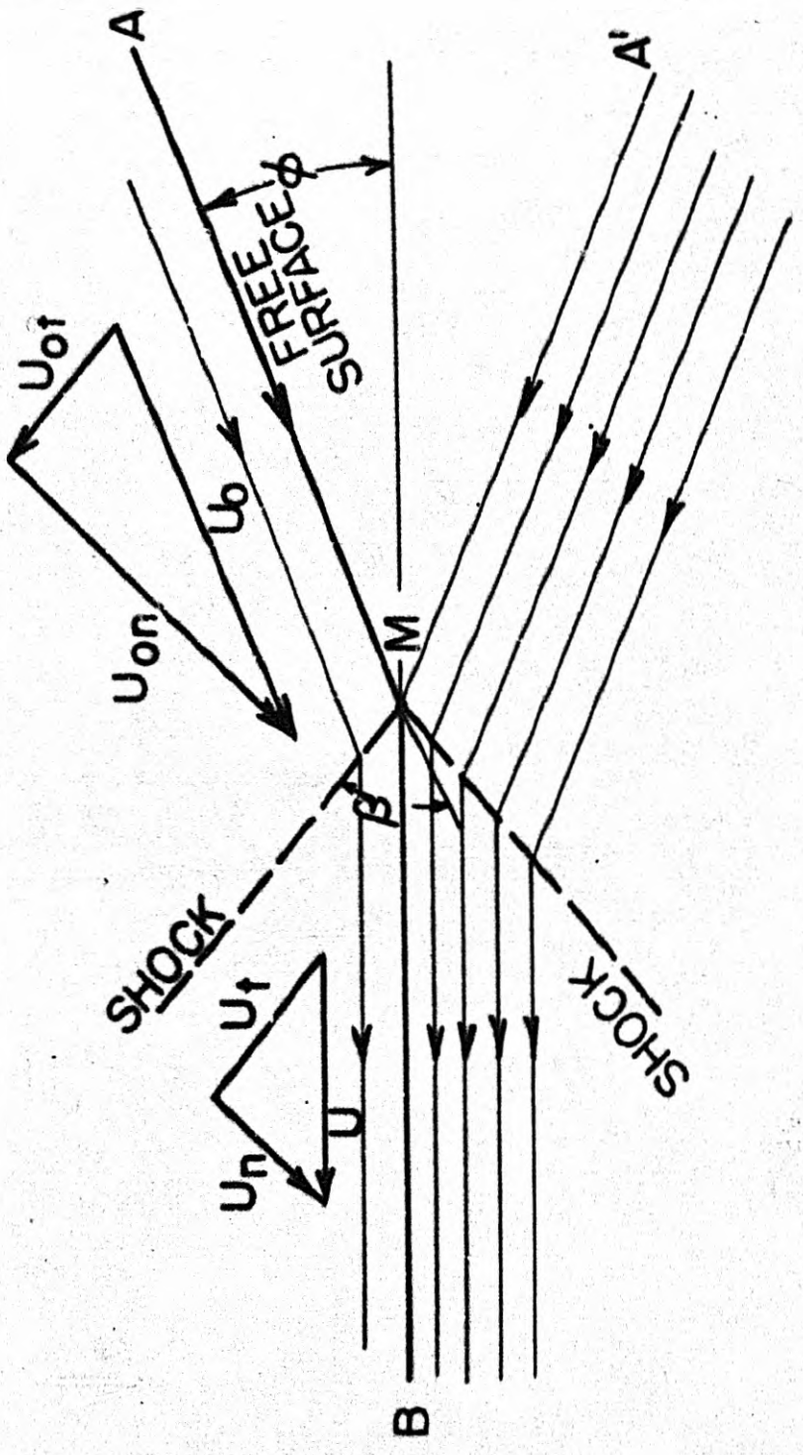

Fig. 2

If U_o is held fixed and ε increased, one reaches a critical angle, ε_c, above which this flow is no longer possible. The following analysis determines the flow configuration for $\varepsilon < \varepsilon_c$ and ε_c as a function ofboth U_o and properties of the colliding material.

Solution of the problem is aided by reference to Fig. 2. Here the initial and final velocities, U_o and U, are resolved into components normal (subscript n) and tangent (subscript t) to the shock wave. Prior to collision, the material is further defined by its density ρ_o and zero pressure. The analysis largely depends upon the mechanical shock equations; i.e. the equation of continuity

$$U_{on} \quad \rho_o = U_n \rho \,, \tag{5}$$

the conservation of momentum perpendicular to the shock front,

$$U_{on} \rho_o (U_{on} - U_n) = P, \tag{6}$$

and the conservation of momentum parallel to the shock front,

$$U_{ot} = U_t. \tag{7}$$

It is convenient to replace Eqns (5), (6) by their explicit solutions for velocity

$$U_{on} = \sqrt{\frac{P(\mu + 1)}{\rho_o \mu}} \tag{8}$$

$$U_n = \sqrt{\frac{P}{\rho_o \mu(\mu + 1)}} \tag{9}$$

where μ is a measure of compression defined by

$$\mu = \frac{\rho}{\rho_o} - 1. \tag{10}$$

Further, by geometry from Fig. 2:

$$U_{ot} = U_t = \sqrt{U_o^2 - U_{on}^2} \tag{11}$$

$$U = \sqrt{U_t^2 + U_n^2} \qquad (12)$$

$$\varphi = \tan^{-1}\frac{U_{on}}{U_t} - \tan^{-1}\frac{U_n}{U_t} \qquad (13)$$

In order to determine the system completely, these equations must be supplemented by equation of state data for the materials concerned. This information, giving pressure behind the shock as a function of μ,

$$P = P(\mu) \qquad (14)$$

is presented and discussed in Appendix I. Use of this relation must be restricted to points P, μ satisfying the shock stability condition

$$\frac{P(\mu+1)}{\mu} \geq \frac{P'(\mu'+1)}{\mu'}, \text{ for } \mu > \mu' > 0. \qquad (14a)$$

From Eqn. (8), this is equivalent to the assertion that a shock wave, to be stable, must have a normal velocity component with respect to the material ahead of the shock which is as great or greater than that for any weaker shock (compression $\mu' < \mu$) into the same medium. Hence it must be imposed to insure stability of the shock wave against decomposition into two or more weaker disturbances which separate as time increases. The condition is satisfied by solidsfor sufficiently strong shocks, since $\frac{P(\mu+1)}{\mu} \to \infty$ as $\mu \to \infty$ and is finite elsewhere. The range of validity of (14a) determines the range of collisions for which this theory is valid.

A simple representation of the problem is that of a shock polar in the hodograph plane(3). It is convenient to take ρ_o and U_o

(3) For a more complete discussion of shock polars see, for example, R. Courant and K. O. Friedrichs "Supersonic Flow and Shock Waves" pp 306-317, Interscience (1948).

as fixed initial conditions for a given polar diagram, while μ is regarded as an independent parameter by variation of which the shock polar is plotted. Values of U_{on} and U_n for given values of μ are obtained by substitution in Eqns (14), (8), (9). Associated values of the remaining variables are computed from Eqns. (11), (12) and (13). A typical plot of these quantities is shown in Fig. 3. The curved locus defines all possible shock transitions associated with a stream of initial velocity U_o and density ρ_o. The parameter μ, not shown in this plot, increases monotonically along the curve, from zero at the right intercept with the ray $\phi = 0$, to a maximum value at the left intercept. Two qualitative features of this shock polar will be assumed true in general: that one and only one critical angle $\left(\frac{d\phi}{d\mu} = 0\right)$ exists and that μ increases monotonically along the curve, i. e. that $\frac{d\phi}{d\mu} > 0$ for $\mu_c > \mu > 0$, $\frac{d\phi}{d\mu} = 0$ at $\mu = \mu_c$, and $\frac{d\phi}{d\mu} < 0$ for $\mu > \mu_c$.

It will be noted that the deflection defined by an angle $\phi < \phi_c$ intersects this curve at two points s and w. Hence this deflection could be caused by either a shock of compression μ_s or μ_w, where $\mu_s > \mu_w$. Although both are compatible with the preceding equations, the former can be discarded by the usual argument of unique continuation: for the limiting case $\phi = 0$, there is no disturbance in the "impinging" streams. Hence the strong shock root s must be discarded, while w is retained. For small angles, then, and, indeed, all angles satisfying $\phi < \phi_c$, the assumption of a continuous behavior

[redacted]

Fig. 2. Shock polar for aluminum,
U_0 = 10 mm/μsec.

[redacted]

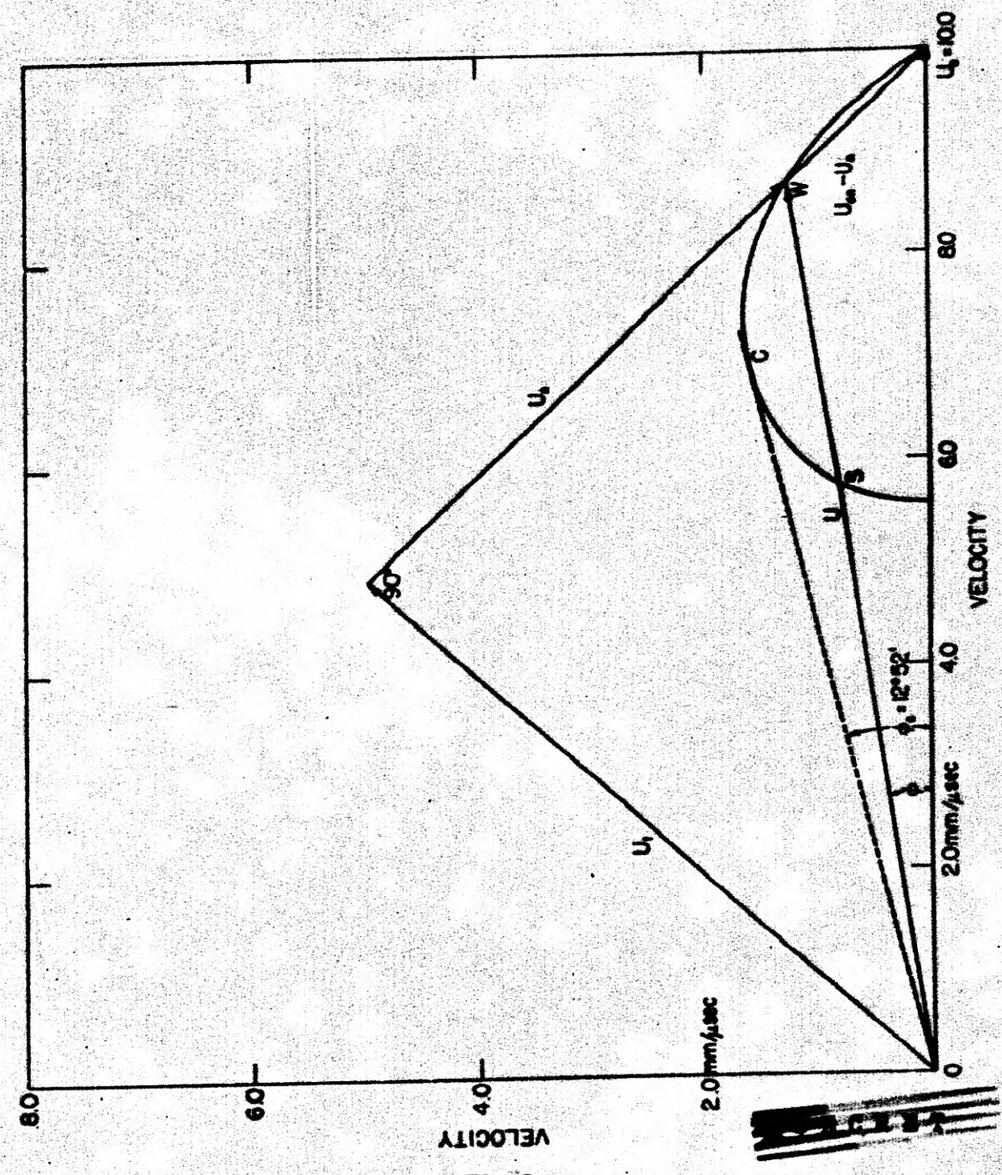
8.0
6.0
4.0
2.0mm/μsec
0
VELOCITY
U_1
U_2
U_{21}
$U_{21}-U_2$
W
C
S
$\phi_1 = 12°32'$
$U_1=100$
80
60
40
2.0mm/μsec
VELOCITY

Fig.3

requires that the weak root w describe the experiment, while s is discarded.

A ray $\beta > \beta_c$ does not intersect the shock polar. The deflection defined by such a ray is therefore not possible by means of a shock, and the above jetless flow cannot occur. Jet-forming collisions will accordingly be associated with such angles. In order to calculate this critical angle, Eqn. (13) can be rewritten

$$\tan \beta = \frac{(U_{on} - U_n)\, U_t}{U^2_t + U_{on} U_n} \qquad (13')$$

or, substituting from Eqns. (8), (9), (11)

$$\tan^2 \beta = \frac{P\left[\rho_o U^2 \left(\frac{\mu}{\mu+1}\right) - P\right]}{(\rho_o U_o^2 - P)^2} . \qquad (15)$$

At β_c, $\frac{d\beta}{d\mu} = \frac{d}{d\mu} (\tan^2 \beta) = 0$. Differentiating, with ρ_o, U_o fixed,

$$\frac{dP}{d\mu} = \frac{P(P - \rho_o U_o^2)}{(\mu + 1)\left[\mu \rho_o U_o^2 - P(\mu + 2)\right]}, \text{ for } \beta = \beta_c. \qquad (16)$$

This relation, together with Eqn. (14) and its derivative with respect to μ, determines the critical values of P and μ for given initial values ρ_o, U_o. The associated critical angle, β_c, is then obtained by substitution in Eqn. (15).

The above calculation is carried out for a range of U_o (subject to the condition that U_o is supersonic). One may then construct a plot for U_o versus β_c. It is more convenient, however, to plot plate velocity in the laboratory system, $V_p = U_o \tan \beta$, versus the

angle 2ϕ. These plots are shown in Figs. 13 and 14 for aluminum and iron. Collisions described by the region above a given critical curve must form jets, while those below the critical curve are assumed jetless, in keeping with the above discussion.

One of the experimental approaches described below employs collisions in which the angle 2ϕ between the free surfaces varies in a continuous manner while plate velocity, V_p, remains effectively constant. A collision at variable ϕ can be regarded as a succession of separate collisions between infinitesimal plane surfaces at constant ϕ, provided a simple criterion is met: The laboratory system velocity of the coalesced plates, immediately behind the shock waves, must not decrease with time, i. e.

$$\frac{d}{dt}\ (V_m - U) \geq 0 \qquad (17)$$

This condition is imposed to insure the non-interaction of successive members of the infinitesimal collisions. In Appendix II, it is shown that (17) is satisfied for $\frac{d\phi}{dt} > 0$ and is violated for $\frac{d\phi}{dt} < 0$. Hence collisions in which the angle 2ϕ between the free surfaces increases with time are described by the above theory, while it is invalid for collisions in which the 2ϕ decreases with time. Fortunately, former case is more important.

It should be noted again that the flow configuration of Fig. 2 is postulated. While it is compatible with the ordinary conservation equations and the properties of solids at high pressures, the question

of its uniqueness and stability has not been proved. It is the purpose of the experiments described below to test predictions of the theory, and of that given in reference (1).

Experiments

Two experimental methods were employed to produce the desired collisions. The first of these is illustrated in Fig. 4. This arrangement uses two identical 12" x 12" plates, the free surfaces of which form a wedge angle 2θ. Each is backed by an 8" x 8" x 2" block of Composition B (60 RDX, 40 TNT), and a plane wave generator[6]. Plate material, the angle 2θ, and plate thickness were varied; all other parameters were held constant, at values indicated in the figure.

The collision process was photographed by a smear camera, through a 1/8" wide slit viewing the median plane of the assembly (see Fig. 4) The direction of sweep of the camera was at 90° to the slit, so that the resulting record is simply a Cartesian space-time plot of motion along the axis of the assembly. The camera used was capable of writing speeds as high as 3.20 mm on film per microsecond.

The high intensity illumination required for such photography

(6) These plane wave generators are a lens-type combination of two explosives with slow and fast detonation velocities, such that point initiation is converted into a plane detonation wave. See J. H. Cook, Research 1, 474 (1948).

Fig. 4. Wedge-type arrangement and smear camera photograph. The photograph illustrated is the 10° collision of two aluminum plates (first line, Table IA).

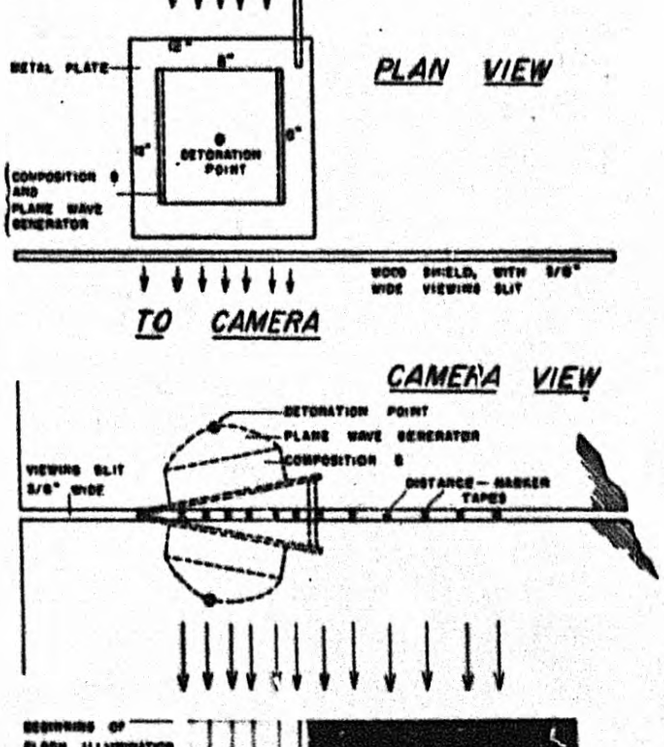
DETORATION POINT
PLANE WAVE GENERATOR
COMPOSITION B
LUCITE
WOOD SHIELD
METAL PLATE
PLAN VIEW
DETORATION POINT
COMPOSITION B AND PLANE WAVE GENERATOR
WOOD SHIELD, WITH 3/8" WIDE VIEWING SLIT
TO CAMERA

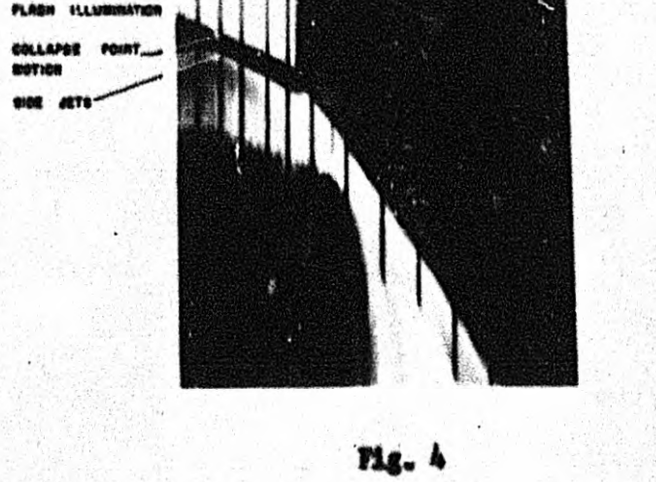
CAMERA VIEW
DETORATION POINT
PLANE WAVE GENERATOR
COMPOSITION B
VIEWING SLIT 3/8" WIDE
DISTANCE — MARKER TAPES

BEGINNING OF FLASH ILLUMINATION
COLLAPSE POINT, BOTTOM
SIDE SETS

Fig. 4

was obtained by means of an argon flash lamp[7], which backlights the wedge region (see Fig. 4) The explosive assembly used to activate this lamp is identical with that which backs each plate.

Simultaneity of detonation[8] can be obtained by using one detonator for all three plane wave generators, with equal lengths of primacord extending from the detonator to each of the three detonation points.

A typical smear camera record is also shown in Fig. 4. Distance (along the axis, from the wedge vertex) increases to the right. Tape distance markers, placed across the slit, serve to identify various positions. Time increases downward, with a zero time arbitrarily defined as the beginning of argon flash illumination. At a later time the light path is obstructed by the impinging walls of the wedge. From the position and slope of this extinction line, one obtains a shadowgraph record of motion along the axis of the wedge. Finally, a jet is produced near the edge of the wedge region, and is observed to proceed to the right. Light necessary for the record of jet motion is produced by self-luminosity of the jet.

A simple auxiliary experiment facilitates intrepretation of the collision record. The trajectory of a single plate when accelerated by the above explosive assembly is examined separately

(7) R. H. Cole "Underwater Explosions". pp 213-14. Princeton University Press (1948).

(8) E. M. Pugh, R. V. Heine-Geldern, J. Foner and E. C. Mutschler. J. Appl. Phys. 22, 487 (1951)

This is accomplished by photographing the motion (in shadowgraph) by means of a Bowen[9] type framing camera, which takes photographs having a time separation of 0.9 microseconds between successive frames. Fig. 5 shows frames selected from such a record. From the motion observed by this method it is a simple matter to calculate the expected motion of the instantaneous point of collision, for two such plates inclined at a given angle. This calculation was carried out for each configuration, and the resulting "predicted collapse" motion was compared with the "observed collapse" from the collision shot. Fig. 5 also shows that the edges of the plate lag behind, while the central region remains effectively plane. This condition causes final stages of the collision to take place at an angle which is greater than the original wedge angle. Near this extreme end one must expect jetting, since the collision angle approaches 180°. It is possible, however, to distinguish between these afterjets and jets associated with collision at the proper wedge angle. Jets from edge effects also arise from the sides of the impinging plates, as may be noted by inspection of Fig. 4. Such jets are directed toward the observer and are identified as luminosity appearing shortly after the collapsing plates have obscured the light from the flash lamp.

---

[9] The Bowen 76 Lens Camera, NOTS, Sept. 1948.

Fig. 5. Framing camera record of brass plate, driven by the explosive assembly shown in Fig. 4. Time separation between pictures is 5.4 μsec, every sixth picture from the original record. Distance between vertical reference wires is six inches.

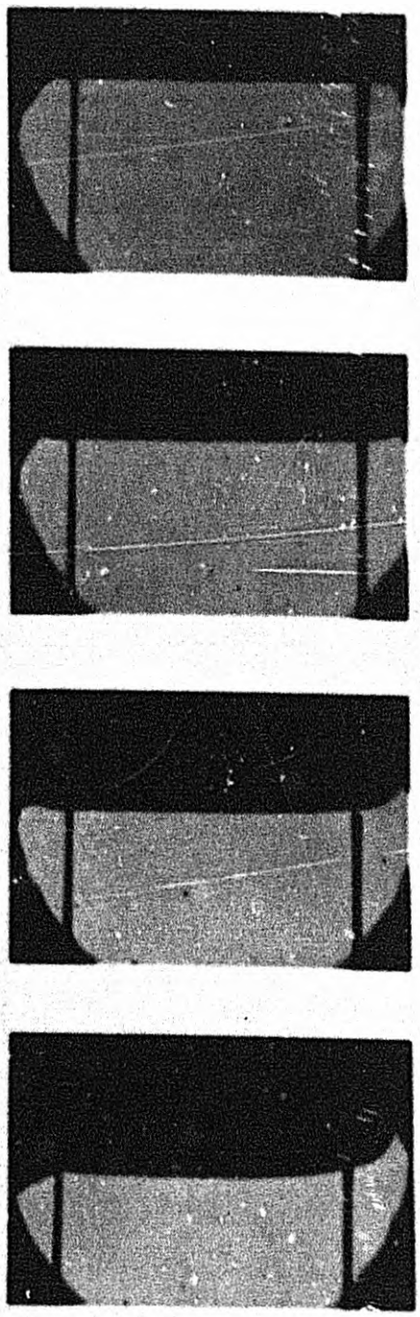

Fig.5

Fig. 6 is a plot of the pertinent features of the photograph shown in Fig. 4. The plates were of dural 1/4" thick and the collapse angle 2ø was 10°. The jetless nature of the collision is readily established: Good agreement between the predicted and the observed collapse is evident. Further, although a jet (actually an afterjet) is present, its velocity is lower than that of the collapse point near the center of the wedge, hence could not have been formed in that region.

Figs. 7 and 8 show the photographic record and data plot for a jet-forming 60° collision of 1/4" dural plates. An accurate determination of the point of origin of the jet is obtained by taking its position and velocity near the open end of the wedge and extrapolating back to the collapse line, as shown in Fig. 8. (Jets are luminous, and motion in the wedge region is observed by shadowgraph, as a result both the jet and collapse point positions become obscure after a jet is formed in the wedge region.) The jet is seen to come from a point before the center of the wedge so that the 60° collision is jet-forming. This extrapolation procedure and the criterion that a jet must have a higher velocity than the moving collision point from which it eminates are sufficient to establish the jet-nojet character of every collision.

Results for shotsfired by the above technique are shown in Table IA.

The second technique employed to produce collisions is shown

Table - IA

Data from Wedge-Type Collisions

Metal	Metal Thickness	Angle between Free Surfaces 2s	Plate Velocity	Results
Dural 24ST 94% Al	1/4"	10°	3.58 mm/μsec	Jetless
	Same	25°	3.58	Jetless
	Same	30°	3.58	Jetless
	Same	34°	3.86	Jet Velocity = 20.17 mm/μsec
	Same	45°	3.86	Jet Velocity = 17.41 mm/μsec
	Same	60°	3.86	Jet Velocity = 13.57 mm/μsec
Steel (mild) 99.5% Fe	Same	25°	2.52	Jetless
	Same	30°	2.52	Jet Velocity = 15.11 mm/μsec
Lead	1/8"	30°	2.30 ± .10	Jetless
	1/4"	45°	2.30 ± .10	Jet Velocity = 11.09 mm/μsec
	1/8"	60°	2.30 ± .10	Jet Velocity = 9.00 mm/μsec
Brass (yellow) 67% Cu 33% Zn	1/4"	10°	2.22	Jetless
	Same	20°	2.22	Jetless
	Same	45°	2.38	Jet Velocity = 12.17 mm/μsec

TABLE IB.

Data from Angle-Variation Collisions

Metal	Plate Thickness	Plate Separation	Charge	Results
Dural 24ST	1/8"	2 cm	8" x 4" x 4" Composition B	Jet at: 2ø = 36° 44' V_p = 4.54 mm/μsec Jet Velocity = 19.33mm/μsec
	1/4"	Same	Same	Jet at : 2ø = 34° V_p = 3.98 mm/μsec Jet Velocity = 17.61mm/μsec
	1/4"	Same	8" x 4" x 4" Baratol	Jet at: 2ø = 24° V_p = 2.08 mm/μsec Jet Velocity = 10.31mm/μsec
Steel	1/8"	Same	8" x 4" x 4" Composition B	Jet at: 2ø = 28° 07' V_p = 2.86mm/μsec Jet Velocity = 15.79mm/μsec
	1/4"	Same	8" x 4" x 4" Baratol	Jet at: 2ø = 18°56' V_p = 1.29 Jet Velocity = 9.21mm/μsec

Fig. 6. Distance-time plot for the 10^8 collision of aluminum plates.

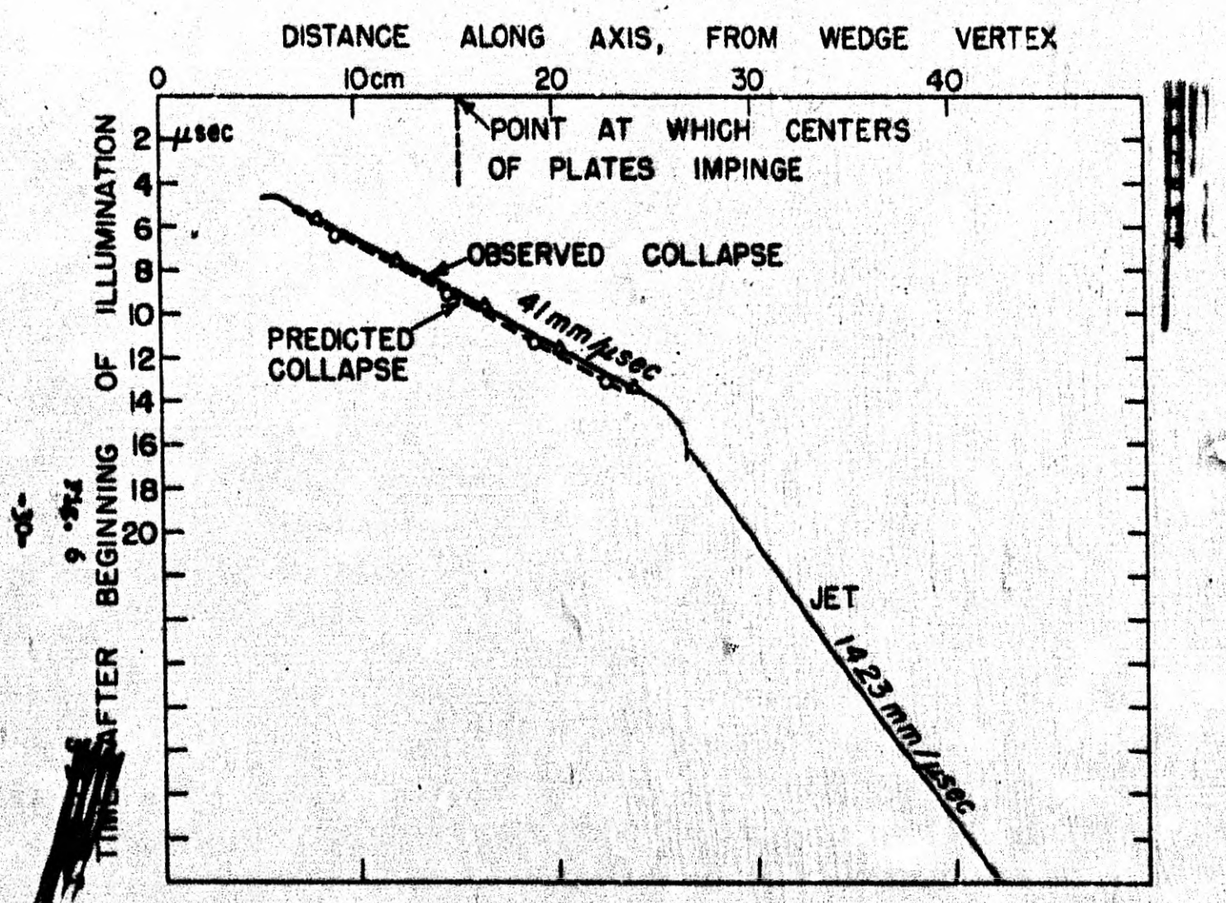
DISTANCE ALONG AXIS, FROM WEDGE VERTEX
0
10cm
20
30
40
POINT AT WHICH CENTERS OF PLATES IMPINGE
OBSERVED COLLAPSE
PREDICTED COLLAPSE
41 mm/μsec
JET
1423 mm/μsec
TIME AFTER BEGINNING OF ILLUMINATION
μsec
2
4
6
8
10
12
14
16
18
20

Fig. 7. Smear Camera record for the 60° collision of aluminum plates (line 6, Table IA).

Fig. 7

Fig. 6. Distance-time plot for the 60° collision of aluminum plates.

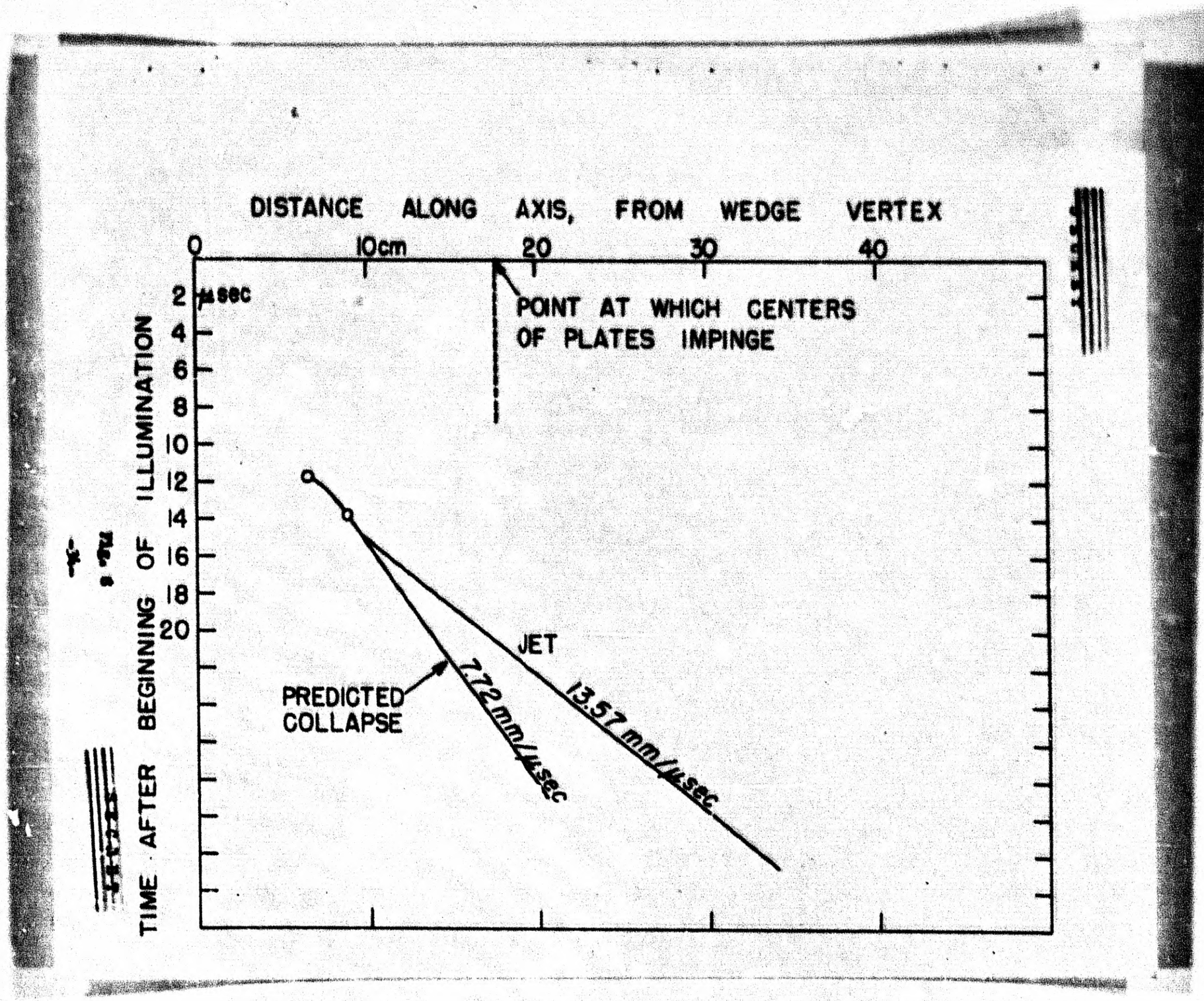
DISTANCE ALONG AXIS, FROM WEDGE VERTEX
0
10cm
20
30
40
POINT AT WHICH CENTERS OF PLATES IMPINGE
TIME AFTER BEGINNING OF ILLUMINATION
2 μsec
4
6
8
10
12
14
16
18
20
JET
13.57 mm/μsec
7.72 mm/μsec
PREDICTED COLLAPSE

in Fig. 9. The plates are aligned and one end of each is backed by an 8" x 4" x 4" block of high explosive, either Composition B or Baratol (75% barium nitrate, 25% TNT). Detonation is accomplished by a small plane wave generator as indicated in the figure. This arrangement gives a continuous range of collision angles, which can be controlled by variation of plate separation and angle between the plates. For the experiments described below, it was convenient to use parallel plates with a two centimeter separation. Plate thickness and material were varied. The photographic procedure (not indicated in the figure) is the same as that for the previous technique.

In order to interpret these experiments it is necessary to know the behavior of one plate when driven by the explosive assembly to be used. This information is again obtained by use of a framing camera which observes plate motion by shadowgraph. Frames from such a record are shown in Fig. 10. The "predicted" collapse point motion is then calculated for the collision of two such plates in a given geometry. The angle of collision is also measured directly from the film. It should be noted that this angle <u>increases</u> throughout the collision, so that $\frac{d\alpha}{dt} > 0$, and that the plate velocity, V_p, is approximately constant. (These conditions are shown, in the theoretical section, to be sufficient to assure applicability of the jetless configuration theory.)

Fig. 9. Angle-variation arrangement and a typical record (experiment listed in line 2, Table IB).

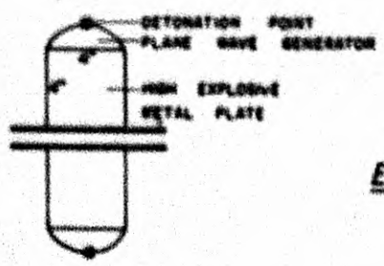

END VIEW

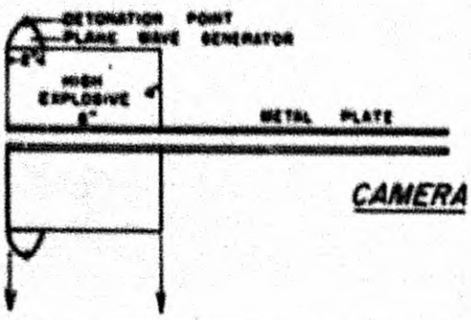

CAMERA VIEW

Fig. 9

Fig. 10. Framing camera record of 1/8" steel plate, driven by charge assembly shown in Fig. 9. Time separation between pictures is 2.7 μsec. Distance between vertical markers is 6".

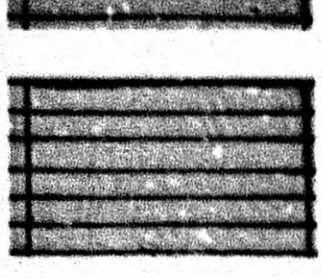

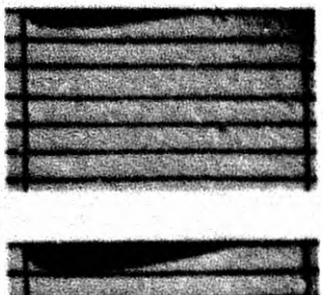

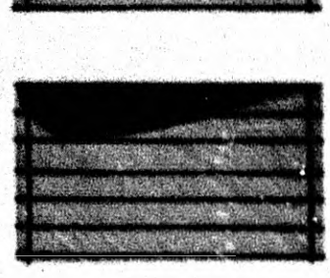

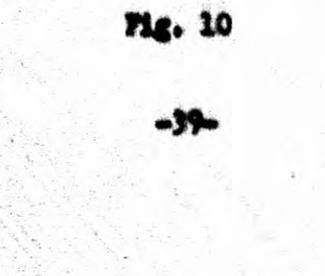

Fig. 10

Fig. 11 shows a plot of the collision photograph given in Fig. 9, together with data obtained from the framing camera record. Observed and predicted collapses are seen to agree closely, until jetting occurs. Values of plate velocity and collision angle at the jetting point are obtained from the framing camera record. Results for shots fired by this technique are shown in Table IB.

An interesting qualitative record of the collision process is shown in Fig. 12. These shadowgraph pictures were taken by a framing camera (0.9 usec between frames) and clearly indicate the jetless nature of early phases of the collision process. This collision used the variable angle technique illustrated in Fig. 9.

Comparison of Theory and Experiments

The jet-noje character of a collision can be compared with predictions of the theory. For this purpose, the alloys used in actual collisions are compared with theoretical curves for their predominant element. Hence 24ST Dural (94% Al) is approximated as aluminum and mild steel (99 + % Fe) is approximated as iron. The lead used in the experiments was essentially pure.

Results for collisions employing dural and steel are compared with their theoretical curves in Figs. 13 and 14, respectively. Points indicate the wedge-type experiments given in Table IA. Angle-variation collisions, taken from Table IB, are plotted as lines. The latter are jetless in early stages and

[redacted]

Fig. 11. Distance-time plot of record shown in Fig. 9, together with "predicted soliton", v and V_p as measured from the framing camera record.

[redacted]

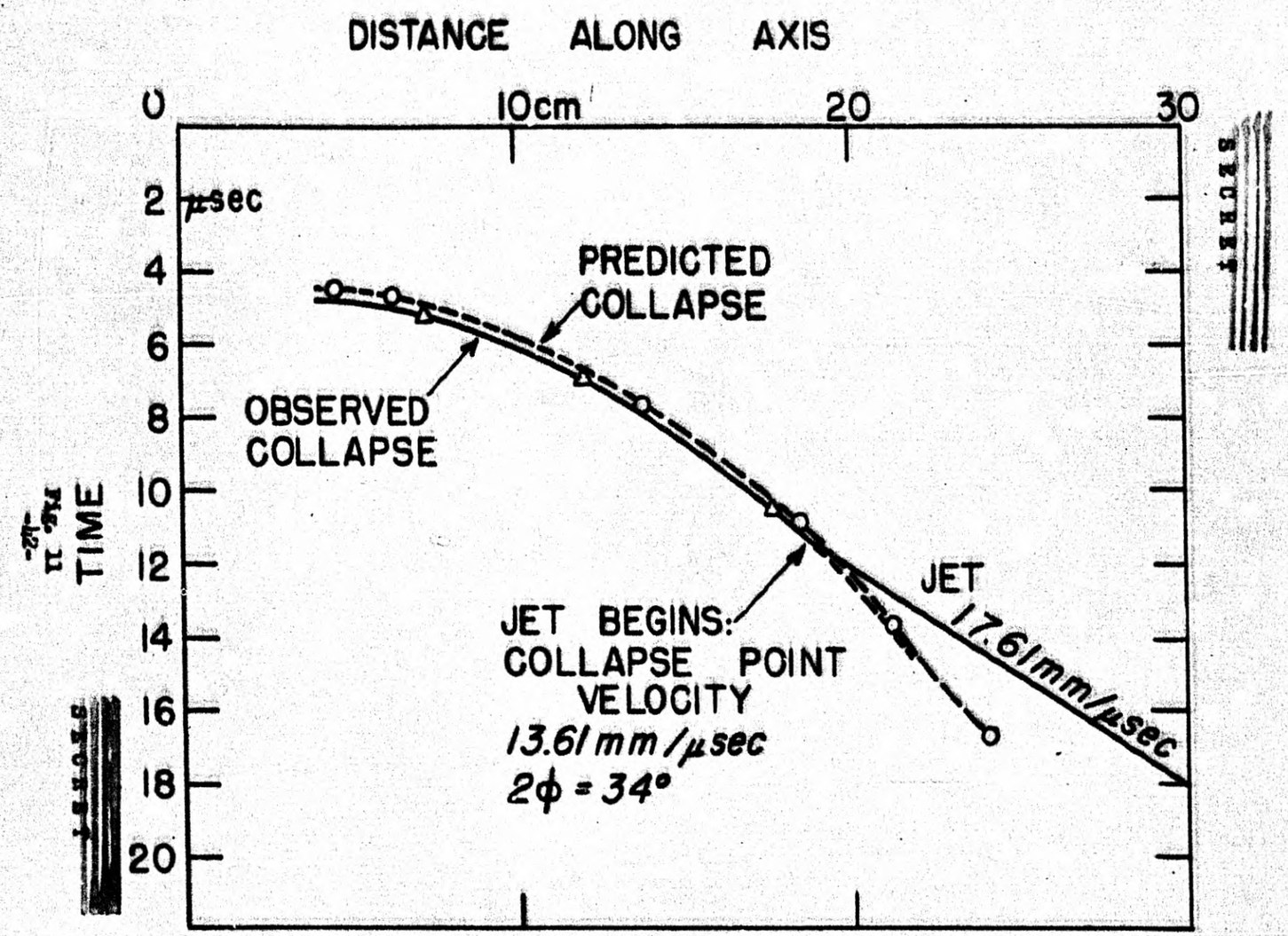
DISTANCE ALONG AXIS
0
10cm
20
30
2
4
6
8
10
12
14
16
18
20
μsec
TIME
PREDICTED COLLAPSE
OBSERVED COLLAPSE
JET BEGINS: COLLAPSE POINT VELOCITY 13.61 mm/μsec
2φ = 34°
JET 17.61 mm/μsec

Fig. 12. The collision of two 1/4" dural plates, 2 cm separation, as recorded by the framing camera. Note jetless nature of early stages of the collision. (Side jets are evident as luminosity following the instantaneous collision point.) Time separation between adjacent pictures is 0.9 μsec, except for the last picture, which is 5.4 μsec later than previous one.

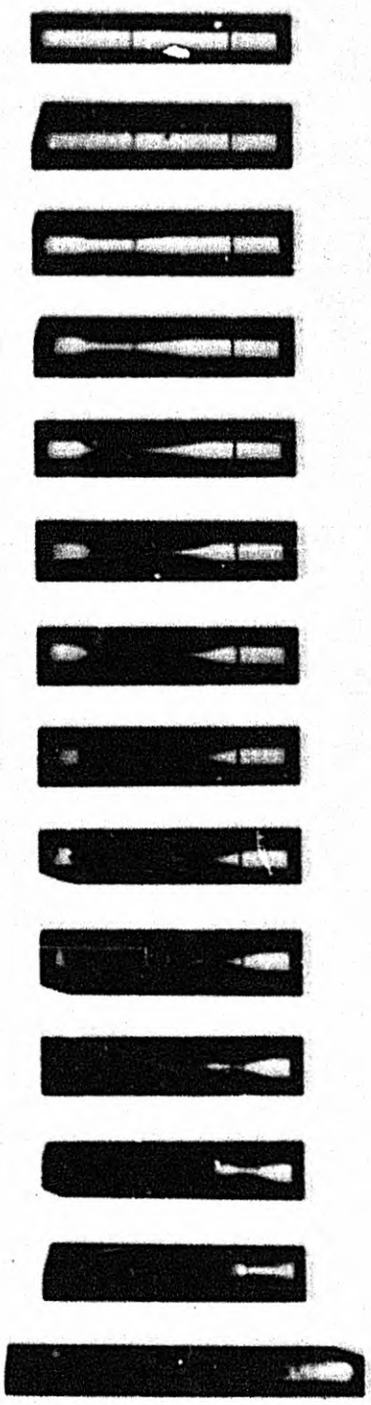

Fig. 12

Fig. 11. Theoretical curve and collision data for aluminum (dural).

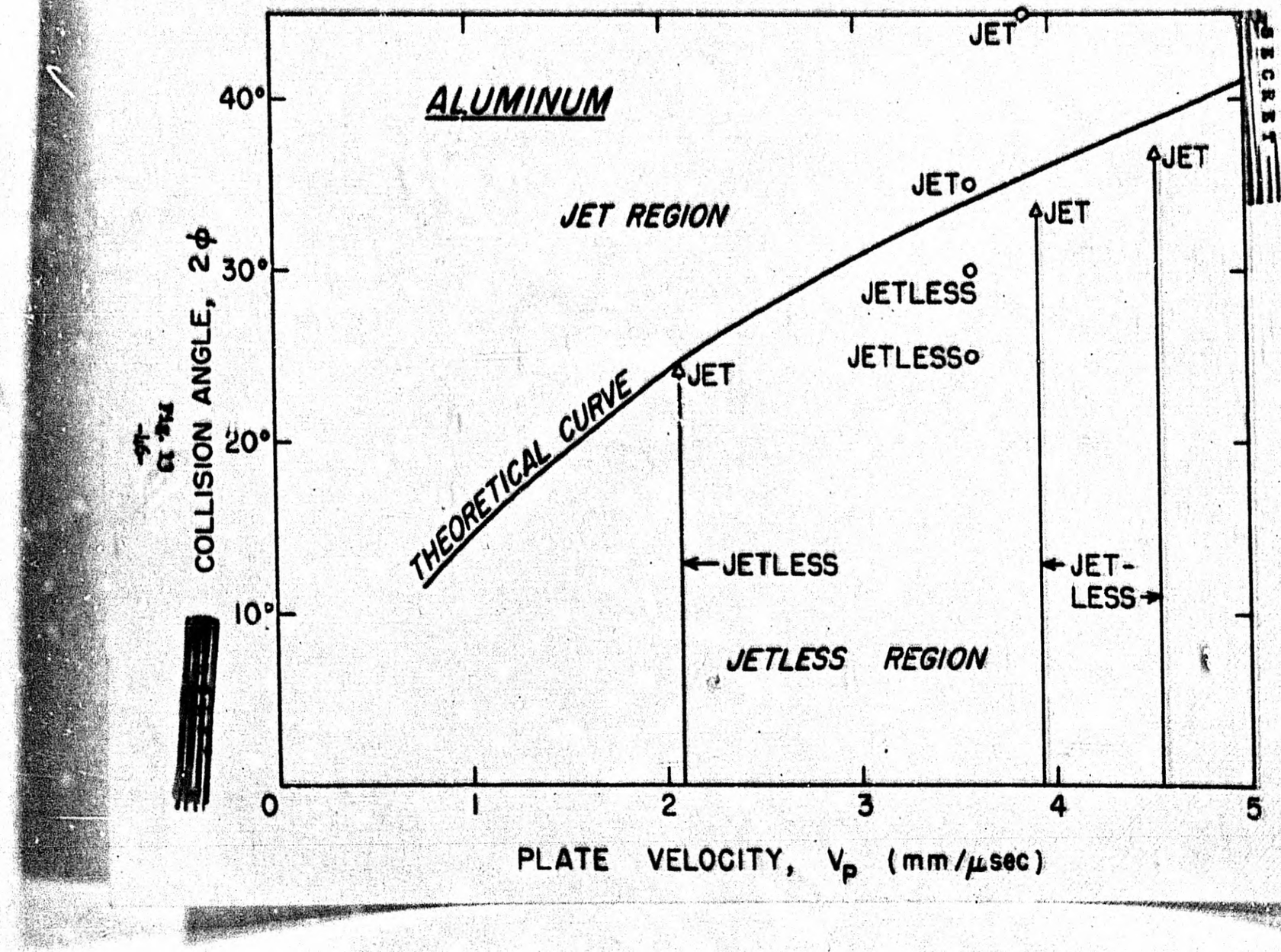
ALUMINUM
JET REGION
JET
JET
JET
JET
JETLESS
JETLESS
THEORETICAL CURVE
JETLESS
JETLESS
JET-
LESS
JETLESS REGION
40°
30°
20°
10°
0
1
2
3
4
5
COLLISION ANGLE, 2φ
PLATE VELOCITY, V_p (mm/μsec)
SECRET

Fig. 11a. Secretest curve and collision data for iron (mild steel).

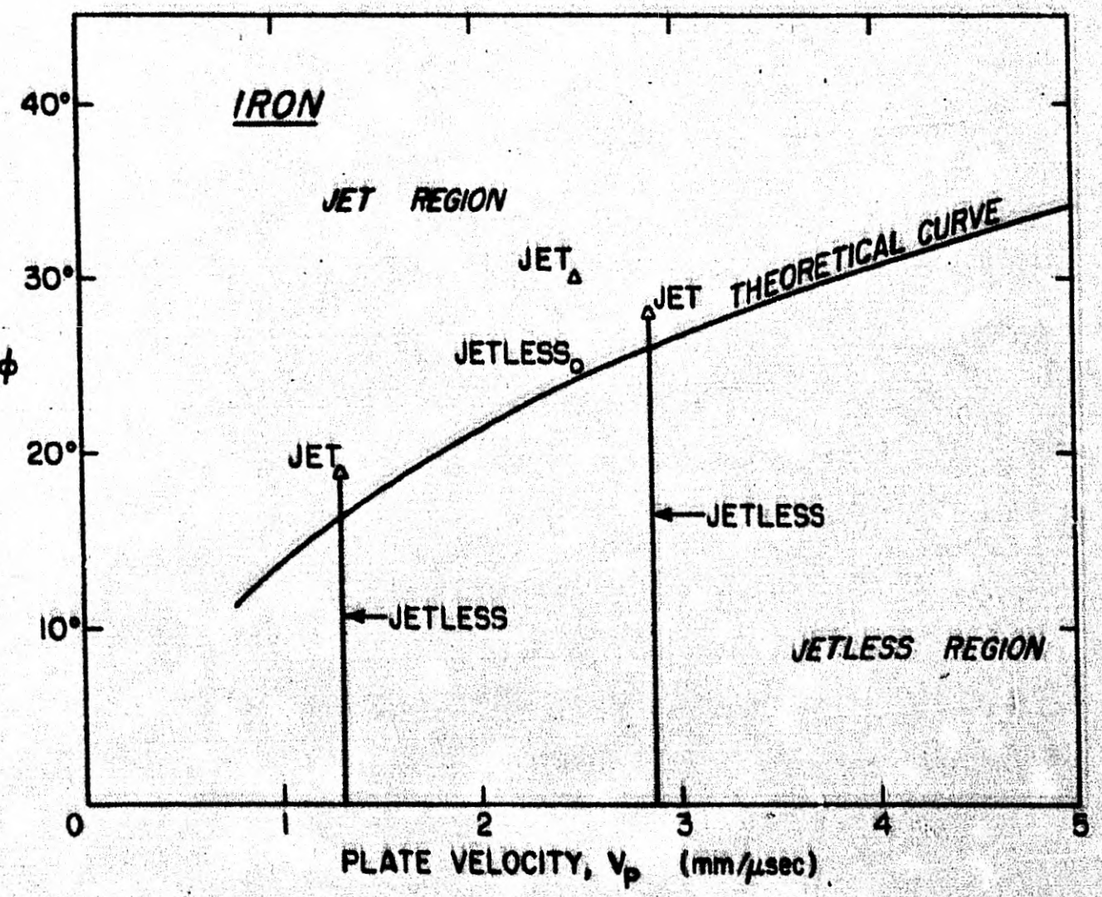

Fig. 14 2φ

each produces a jet within 3° of the theoretical value of $2\theta_c$; aluminum is seen to jet slightly below the theoretical curve and iron jets slightly above. These trends, different for aluminum and iron, seem to suggest that most of the existing error is due to equation-of-state approximations. The wedge-type experiments are seen to be jetless if they lie below the theoretical curve and jet-forming above, with an exception in the case of the 25° iron collision which was jetless. This collision could also be made to agree by shifting the theoretical curve for iron upward some 2°, as suggested by the results of the angle-variation collisions. Wedge-type experiments for lead and brass are also listed in Table IA. The 30° collision for lead was jetless, while 45° and 60° collisions produced jets; these results are in agreement with theory, which indicates a critical angle of 36°. Lead free surfaces, when accelerated by high explosives, emit a spray of lead (presumably of low average density). This spray makes free surface motion difficult to observe and permitted only a crude bracketing of the theoretical curve. Three brass (67% copper, 33% zinc) collisions, at 10°, 20° and 45°, are reported in Table IA. The first two are jetless and the 45° collision formed a jet, indicating the existence of a jetless configuration and a critical angle for brass (These results would be predicted for pure copper.. Equation of state data for brass are not available at present.).

The above agreement between theory and experiments may be regarded as the necessary experimental verification of the jetless flow configuration postulated in the theory section.

When jets are observed, their velocities can be compared with the predictions of reference (1). This is done in Fig. 15 where jet velocities reported in Table IA are plotted and compared with Eqn. (1). Experimental results are seen to agree closely with theory for the wide-angle collisions. The collisions which take place at angles only slightly greater than the critical angle, however, produce jets which are slower than those indicated by the theoretical curve.

Concluding Remarks

The extension to asymmetric collisions of the preceding theoretical and experimental work is straightforward. The postulated jetless flow, analagous to that shown in Fig. 2, is demonstrated in Fig. 16. Pressure must be constant across the contact surface which separates the two dissimilar streams, and the flow component normal to this surface must be zero. The velocity components parallel to this surface may be unequal, however, so that a slipstream results. From Eqns. (14) and (15), the angle of flow deflection for a given stream may be regarded as a function of shock pressure. Then

$$2\theta(P) = \theta_1(P) + \theta_2(P)$$

for the jetless configuration. A breakdown of the jetless configuration occurs when either $\theta_1(P)$ or $\theta_2(P)$ reaches the critical angle associated with that stream. The critical angle between the free surfaces is then given by

$$2\theta_c(P_c) = \theta_1(P_c) + \theta_2(P_c)$$

Fig. 15. Theoretical jet velocity curve and experimental data from Table IA.

SECRET

Fig. 13

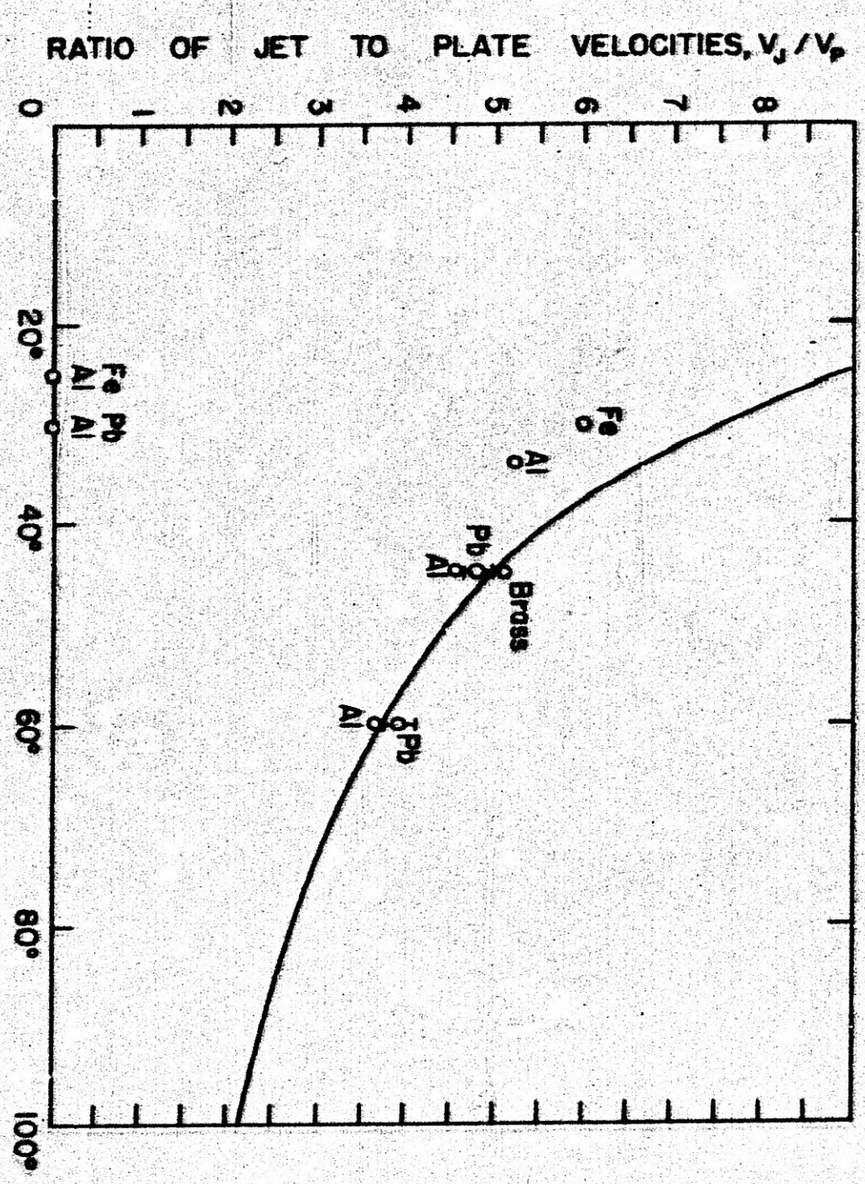

SECRET

Fig. 16. Jetless configuration for the asymmetric collision (unlike materials, unequal velocities).

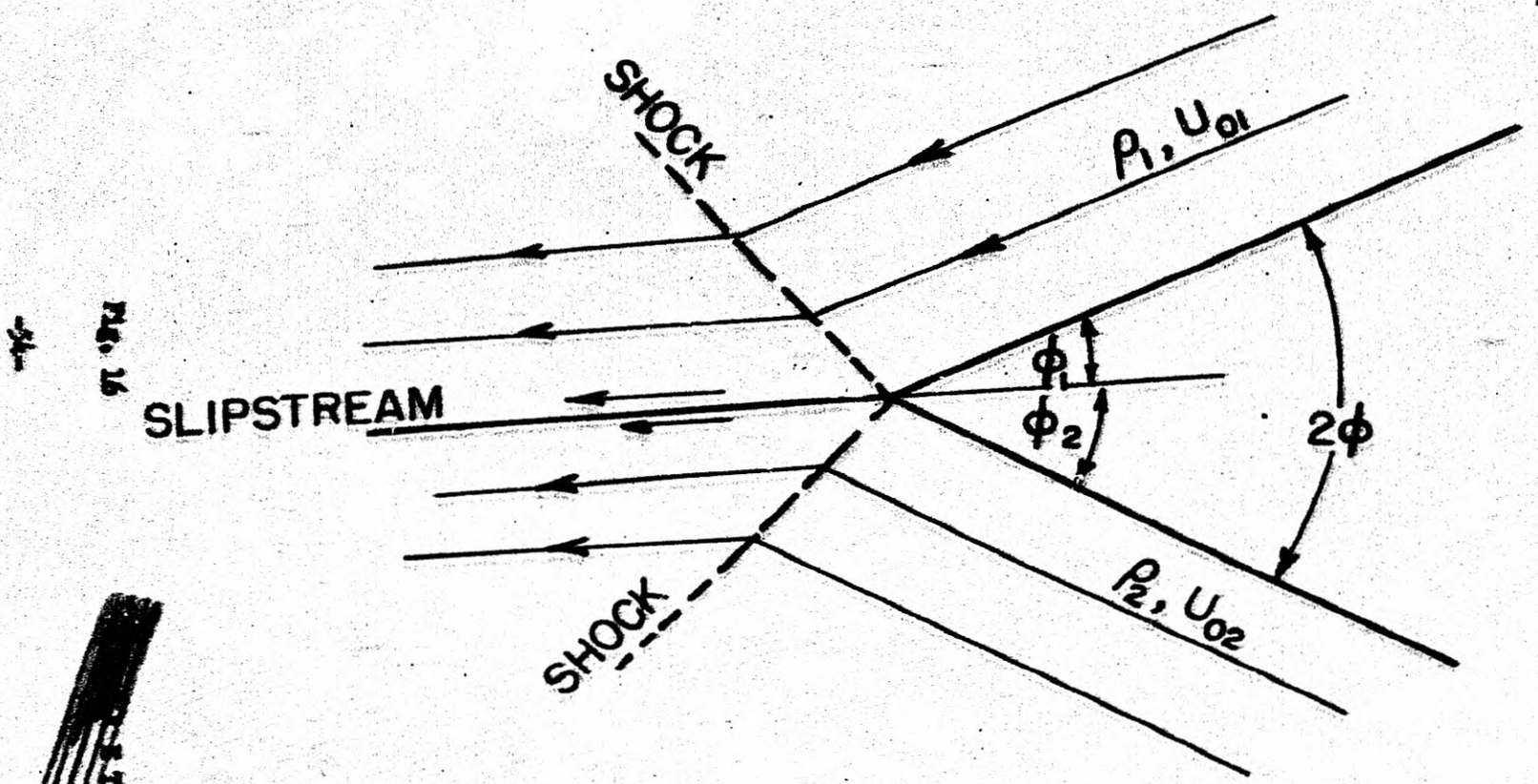
SHOCK
ρ_1, U_{01}
SLIPSTREAM
ϕ
ϕ_2
2ϕ
SHOCK
ρ_2, U_{02}

where P_c is the shock pressure associated with maximum possible deflection of either stream 1 or 2, whichever is smaller, and is given by direct calculation from Eqn. (16).

An experimental study of asymmetric collisions would require the use of a viewing slit which runs along the expected path of the collision point. This path could beaccurately predicted from known trajectories of the plates. Difficulties might arise, however, if the jet produced did not remain in the viewing field defined by the slit. In any case, a framing camera record, of the type shown in Fig. 12, could be used to record the collision.

Appendix I.

Equation of State Data for Al, Fe and Pb.

Equation of state data are obtained from tables compiled by N. Metropolis at the Los Alamos Scientific Laboratory. A relation between shock pressure P and compression $\mu = \frac{\rho}{\rho_0} - 1$ of the form

$$P = \frac{a\mu + \beta\mu^2 + \gamma\mu^3 + \delta\mu^4 + \varepsilon\mu^5}{1 + 1.5\mu^2}$$

was assumed, where α, β,... are parameters characteristic of a given metal, making possible a five point fit with data. Two such points, extending to pressures of about 0.04 megabars, were taken from Birch's Handbook of Physical Constants. The remaining three points, in the region of 75 megabars, were calculated from a generalized Fermi-Thomas model of the atom[4]. Resulting values of the parameters are listed in the accompanying table[5].

Metal	a	β	γ	δ	ε
Aluminum	0.733	1.190	0	2.380	0
Iron	1.6832	2.275	12.362	7.7665	.3741
Lead	0.42481	1.67146	3.65693	1.23617	0.32732

(4) R. P. Feynman, N. Metropolis, and E. Teller, "Equation of State of Elements Based on the Generalized Fermi-Thomas Theory". Phys Rev. 75, 1561 (1949).

(5) The P-μ relations resulting from use of these parameters satisfy the shock stability condition (14a), even for very weak shocks. This is brought about by use of data points produced by uniform hydrostatic pressures. While this pressure is undoubtedly the only one of importance for extremely strong shocks, a study of weak disturbances requires consideration of stresses which result from strength of material, giving rise to a violation of (14a).

Appendix II.

To show $\frac{d}{dt}(V_m - U) \gtrless 0$ for V_p constant and $\frac{d\sigma}{dt} \gtrless 0$.

Consider

$$\frac{d}{d\sigma}(V_m^2 - U^2)$$

where, from Fig. 1

$$V_m = \frac{V_p}{\sin \sigma}.$$

and from Fig. 2

$$U^2 = U_t^2 + U_n^2 = U_o^2 - U_{on}^2 + U_n^2$$

$$= \frac{V_p^2}{\tan^2 \sigma} - (U_{on}^2 - U_n^2)$$

But $U_{on}^2 - U_n^2 = \frac{P}{\rho_o} \frac{\mu + 2}{\mu + 1}$ by combination of Eqns. (8) and (9).

Substituting:

$$\frac{d}{d\sigma}(V_m^2 - U^2) = \frac{d}{d\sigma}\left[V_p^2 + \frac{P(\mu + 2)}{\rho_o(\mu + 1)}\right] = \frac{1}{\rho_o}\frac{d}{d\sigma}\left[P\frac{\mu + 2}{\mu + 1}\right]$$

Equivalently,

$$\frac{d}{d\sigma}(V_m^2 - U^2) = \frac{1}{\rho_o}\frac{du}{d\sigma}\frac{d}{d\mu}\left[P\frac{\mu + 1}{\mu} \cdot \frac{\mu(\mu + 2)}{(\mu + 1)^2}\right]$$

$$= \frac{1}{\rho_o}\frac{du}{d\sigma}\left[\frac{\mu(\mu + 2)}{(\mu + 1)^2}\frac{d}{d\mu}\left[\frac{P(\mu + 1)}{\mu}\right] + \frac{P(\mu + 1)}{\mu}\frac{d}{d\mu}\left[\frac{\mu(\mu + 2)}{(\mu + 1)^2}\right]\right],$$

which is positive since (1.1a), when μ' is made to approach μ_s implies $\frac{d}{d\mu}\frac{P(\mu + 1)}{\mu} \geq 0$, and $\frac{du}{d\sigma} > 0$ is assumed valid for the weak root

of all shock polars (see page 14). Hence

$$\frac{d}{d\theta}(V_n^2 - U^2) = V_n \frac{dV_n}{d\theta} - U\frac{dU}{d\theta} > 0.$$

Dividing by U,

$$\frac{V_n}{U}\frac{dV_n}{d\theta} - \frac{dU}{d\theta} > 0.$$

But, from Fig. 1, $V_n > U > 0$ and $\frac{d}{d\beta}(V_n) = \frac{d}{d\theta}\frac{V_p}{\sin\theta} < 0.$

Hence $$\frac{dV_n}{d\theta} - \frac{dU}{d\theta} = \frac{d}{d\theta}(V_n - U) < 0,$$

and we conclude

$$\frac{d}{dt}(V_n - U) = \frac{d\theta}{dt}\frac{d}{d\theta}(V_n - U) \gtrless 0 \text{ for } \frac{d\theta}{dt} \gtrless 0.$$